DOI: 10.1002/((please add manuscript number))
Article type: Communication

Rational Design of High-Concentration Ti^{3+} in Porous Carbon-Doped TiO_2 Nanosheets for Efficient Photocatalytic Ammonia Synthesis

Qing Han, Chongbei Wu, Haimiao Jiao, Ruoyu Xu, Yuze Wang, Jijia Xie, Qian Guo, Junwang Tang**

Dr. Q. Han, C. B. Wu, Y. Z. Wang
Key Laboratory of Cluster Science
Key Laboratory of Photoelectronic/Electrophotonic Conversion Materials
Department of Chemistry and Chemical Engineering
Beijing Institute of Technology
Beijing 100081, China
E-mail: qhan@bit.edu.cn
Dr. Q. Han, H. M. Jiao, R. Y. Xu, J. J. Xie, Prof. J. W. Tang
Solar Energy Group, Department of Chemical Engineering
University College London
Torrington Place, London, WC1E 7JE, United Kingdom.
E-mail: junwang.tang@ucl.ac.uk
Q. Guo
Queen Marry of London University

Keywords: porous carbon-doped TiO_x nanosheets, high-concentration Ti^{3+}, bottom-up strategy, visible light, photocatalytic ammonia synthesis

The photocatalytic ammonia synthesis is exciting but quite challenging with a very moderate yield at present. One of the greatest challenges is to develop highly active centers in a photocatalyst for N_2 fixation under ambient conditions. Herein, a porous carbon-doped anatase TiO_x (C-TiO_x) nanosheets with high-concentration active sites of Ti^{3+} are presented, which was produced by layered Ti_3SiC_2 through a reproducible bottom-up approach. It is shown that the high-concentration Ti^{3+} sites are major species for the significant increase in N_2 photoreduction activity by the C-TiO_x. Such bottom-up substitutional doping of C into TiO_2 is responsible for both visible absorption and generation of Ti^{3+} concentration. Together with the porous nanosheets morphology and the loading of a Ru/RuO_2 nanosized cocatalyst for enhanced charge separation and transfer, the optimal C-TiO_x with a Ti^{3+}/Ti^{4+} ratio of 72.1% shows a high NH_3 production rate of 109.3 umol g^{-1} h^{-1} under visible-light irradiation and a remarkable apparent

quantum efficiency of 1.1% at 400 nm, which is the highest compared to all TiO_2-based photocatalysts at present.

Ammonia (NH_3) is an important chemical raw material that plays a significant role in the synthesis of fertilizers, explosives, fibers, and plastics. It has been identified as a suitable hydrogen carrier because of its high energy density and liquefiable feature.[1,2] Traditionally, NH_3 is synthesized using the Haber–Bosch process, which requires high temperature and pressure to dissociate the extremely strong N≡N bonds of N_2.[3,4] Moreover, the generation of H_2 required for this process causes the emission of large amounts of CO_2.[5] On the other hand the photocatalytic reduction of N_2 can be performed at ambient temperature and atmospheric pressure using water as the proton source , it is considered to be a promising NH_3 production method.[6-10] Hence, the development of highly active and stable photocatalysts has attracted numerous attentions of researchers over the past decade. To date, some precious metal catalysts (*eg.*, Au, Ru) and various semiconductors, including ZnO, BiOBr and $W_{18}O_{49}$, boron nitride, layered double hydroxides, and graphitic carbon nitride have been studied as active photocatalysts for the reduction of N_2.[11-21] With these advances in mind, the photocatalytic NH_3 production rate is currently still hindered by its slow reaction kinetics and low efficiency.

Previous researchers have claimed that the oxygen vacancies (OVs) present in transition metal oxides were the active sites for the reduction of N_2, as reported by Li *et al.*.[22] They found that the OVs on the (110) surface of TiO_2 were the catalytic centers for the chemisorption and activation of N_2 during the photoreduction of N_2. Recently, Hirakawa *et al.* have shown that the surface Ti^{3+} species of rutile TiO_2 had the potential to increase the donation of electrons to the anti-bonding π^* orbitals of N_2,[23] which could serve as the active sites to effectively weaken and promote the cleavage of the N≡N bonds.[6,18] Nevertheless, Comer *et al.* performed theoretical calculations and reported that the reduction of N_2 could not occur on the (110) surface of rutile TiO_2.[25] Up to now, all the reported TiO_2-based photocatalysts for NH_3

synthesis have mainly focused on the creation of OVs on TiO_2 as the photocatalysts, overlooking the real Ti^{3+} active sites and their relationship with the performance of photocatalytic NH_3 synthesis. Interestingly, recent modelling findings clearly indicated that two adjacent Ti^{3+} sites of anatase TiO_2 could chemically adsorb and activate N_2, [26] which was assessed by electrocatalytic N_2 reduction on the optimal Zr-doped TiO_2 with a $Ti^{3+}/\Sigma Ti$ ratio of 31%. This indicates that controlling the concentration of Ti^{3+} ions in TiO_2 to obtain such functional adjacent Ti^{3+} sites would be a crucial aspect in either electrocatalysis or photocatalysis. Taking this advance, there is not a report on this adjacent Ti^{3+} sites used in photocatalytic photocatalytic N_2 reduction.

Recent computational results also showed that carbon doping in TiO_2 could not only promote the cleavage of the N≡N bond,[27] which is the rate-determining step for the reduction of N_2, but also reduce the band gap of TiO_2, and thus allowing it to harvest visible light.[28] Moreover, the substitutional dopants of TiO_2 would inherently create Ti^{3+} ions, which might be served as the active centers as predicted above for the chemisorption and activation of N_2.[29] These combined advantages render C-doped TiO_2 to be an excellent candidate catalyst for the NH_3 production. Additionally, the introduction of heteroatoms in metal oxides, including TiO_2, has been mainly achieved using top-down/post-treatment approaches, which usually suffers from confined thermo-dynamic solubility of dopants substitution in the bulk and dopants-related recombination centers,[24,28,30] thus leading to poor catalytic activity. In contrast, the bottom-up strategy could be used to well control the solubility of substitutional dopants in the bulk, and it is a robust and reproducible approach for building defined structures.[31,32] Therefore, the development of a facile and effective bottom-up method to synergistically control the solubility of the substitutional dopants in TiO_2 and their ability to construct nanoarchitectures is very crucial yet challenging. On the other hand, a layered precursor used for catalyst synthesis would generate a large surface area which can provide abundant active site. In this regard, MAX phases are interesting candidate precursors, which are a class of ternary layered carbides and

nitrides, with the general formula $M_{n+1}AX_n$, where M represents transition metal (n is 1, 2 or 3) and A stands for the groups IIIA and IVA elements, X represents carbon or nitrogen.[33,34] Recently, it was reported that MAX could be a promising materials to be used as self-sacrificing compound for preparing photocatalysts, which exhibited enhanced photocatalytic activity due to the layered structure with improved surface area, the formation of hybrid structure with facilitated charge separation, or the generation of the OVs in materials serving as the reactive sites.[35-40] However, there is no report on investigation of MAX as the specific precursor to doped carbon into TiO_2 porous nanosheets with finely-tuned Ti^{3+} concentration.

Herein we report a simple bottom-up method by using layered Ti_3SiC_2 MAX as the specific precursor for the production of C-doped anatase titanium oxide (C-TiO_x) nanosheets with high-concentration Ti^{3+} species. The layered Ti_3SiC_2 served as the structure-directing template, source of dopant C and source of Ti for the formation of porous C-doped TiO_x, which was subsequently used as the photocatalyst for the synthesis of NH_3. The high-concentration Ti^{3+} on the synthesized C-TiO_x could significantly chemisorb and activate N_2 molecules. Moreover the NH_3 production activity was well correlated with the amount of Ti^{3+}, which could be easily tuned by adjusting the material syntehsis conditions. In addition, C dopants redshifted its absorption edge toward the visible region and TiO_x still maintained its stability. Furthermore, the porous C-TiO_x nanosheets had large surface area which could provide plenty of N_2 adsorption sites and multielectron transfer channels. Moreover, the introduction of Ru/RuO_2 nanoparticles onto C-TiO_x could synergistically reduce the charge recombination and catalyze the reduction of N_2, which would allow the optimal C-TiO_x to exhibit remarkably high N_2 reduction performance, i.e.109.3 μmol g^{-1} h^{-1} of NH_3 production rate under visible light irradiation and 1.1% of the apparent quantum efficiency at 400 nm .

Typically, C-TiO_x could be obtained *via* H_2O_2-assistant thermal-oxidation etching (H_2O_2-TOE) strategy (**Figure 1a**), where the etching of the Si layer of black Ti_3SiC_2 in H_2O_2 solution at 200 °C for 4 h to weaken the interactions between the layers and simultaneously oxidize the

exposed Ti and C. This led to the formation of a primrose yellow product denoted as C_4-TiO_x, which could be well dispersed in water, and was required for the reduction of N_2 in water. The scanning electron microscopy (SEM) revealed that Ti_3SiC_2 presented closely compacted layered structure (**Figure S1a**), and its morphology was altered to porous nanosheets (**Figures 1b, S1b**) after the H_2O_2-TOE treatment. The high-resolution transmission electron microscopy (HRTEM) image of C_4-TiO_x (**Figure S2**) further revealed that the obtained sample presented partial short-range order. The lattice fringes with the *d*-spacing of 0.351 nm were assigned to the (101) surface of anatase TiO_2, which confirmed the formation of anatase TiO_2.[31] Element mapping revealed the coexistence and uniform distribution of Ti, O, and C in the structure of C_4-TiO_x (**Figure 1c**).

To further confirm the structure of the H_2O_2-TOE-obtained powders, their X-ray diffraction (XRD) patterns and Raman spectra were obtained and analyzed. For comparison, C_4-TiO_x was directly annealed at 600 °C for 2 h in air, and the obtained compound was denoted as TiO_2-air. The six dominant peaks at 25.5°, 37.9°, 48,3°, 53.9°, 55.3°, and 62.8° observed in the XRD spectrum of TiO_2-air (**Figure 2a**) were well indexed to anatase TiO_2 (JCPDS 21-1271),[28,32] which confirmed the formation of anatase TiO_2 *via* the high-temperature annealing of C_4-TiO_x. The peak at approximately 60° in the XRD pattern of C_4-TiO_x disappeared (**Figure 2a**) after annealing, which suggested the complete delamination of Ti_3C_2 and no crystallographic stacking of the Ti_3C_2 sheets.[33,34] By contrast with the most intense peak in the XRD spectrum of TiO_2-air, which was observed at 25.5°, a slightly shifted peak at approximately 25.3° was detected in C_4-TiO_x and was attributed to the replacement of O by C.[28] The other four peaks that are typically assigned to anatase TiO_2 were also observed in the XRD pattern of C_4-TiO_x,[29] however, they were much weaker than the corresponding peaks in the XRD pattern of TiO_2-air, and were slightly shifted toward smaller angles. These results were in good agreement with the HRTEM images and further confirmed the formation of anatase TiO_2 with low degree of crystallinity. The peaks at 146, 394, 524, and 638 cm^{-1} in the Raman spectrum of TiO_2-air

(**Figure 2b**) were attributed to the E_g, B_{1g}, A_{1g}+B_{1g}, and E_g modes (*) of anatase TiO_2, respectively,.[6,28] The Raman spectrum of C_4-TiO_x is similar to that of TiO_2-air, further confirming that the short range of crystallinity anatase TiO_2 structure. In addition, the peaks of the D and G vibration modes of graphite, which are typically located at approximately 1400 and 1600 cm^{-1}, could not be detected in the Raman spectrum of C_4-TiO_x (**Figure S3**), thus suggesting the loss of the C layer. Moreover, the presence of the noticeable peaks (◆) ascribed to the vibration of the Ti–C bonds in the Raman spectra of C_4-TiO_x (**Figure 2b**) indicated that C_4-TiO_x still contained C dopants,[32-34] implying that C-doped TiO_x formed via H_2O_2-TOE.

X-ray photoelectron spectroscopy (XPS) analysis was further conducted to study the oxidation states of the metal ions on the catalyst surfaces (**Figure S4a**). The Ti 2*p* XPS profile (**Figure 2c**) showed two predominant Ti $2p_{3/2}$ and Ti $2p_{1/2}$ peaks at 458.9 and 464.6 eV, respectively, which were ascribed to anatase TiO_2.[24] These two peaks could be further deconvoluted into four subpeaks at 457.4eV, 459.2, 463.1, and 464.9 eV, which were assigned to Ti^{3+} $2p_{3/2}$, Ti^{4+} $2p_{3/2}$, Ti^{3+} $2p_{1/2}$, and Ti^{4+} $2p_{1/2}$,[24,32] respectively, and confirmed the coexistence of Ti^{3+} and Ti^{4+} species at different ratios depending on the synthesis conditions (*vide infra*). In addition, the presence of the two small Ti^{2+} peaks at 455.9 and 461.5 eV, which were attributed to Ti-C bonds in the Ti *2p* XPS profile of C_4-TiO_x confirmed the presence of the C dopants in the structure of C_4-TiO_x.[34,35] The O *1s* XPS profile (**Figure S4b**) of C_4-TiO_x was deconvoluted into four peaks at 530.1, 531.1, 532.3, and 533.3 eV, which were assigned to the Ti–O bonds (30.58%), Ti–OH bonds (12.96%), OVs (41.27%), and adsorbed O species (15.2%), respectively.[24] X-ray absorption near-edge fine structure spectroscopy (XANES) was further used to analyze the structure of C_4-TiO_x. The results of the Ti K-edge XANES analysis (**Figure 2d**) indicated that the edge energy of Ti in C_4-TiO_x was significantly higher than that in Ti_3SiC_2, which suggested that the Ti atoms in C_4-TiO_x were successfully oxidized.[35] The shape of the XANES profile of C_4-TiO_x coincided with the reference one of anatase TiO_2, which further confirmed the formation of anatase TiO_2. The absorption edge energy of C_4-TiO_x was slightly

lower than that of TiO_2, which indicated that the average oxidation state of the Ti^{4+} species decreased.[33] These results suggested that the oxidation state of the titanium species in the bulk of C_4-TiO_x were on average lower than those in TiO_2, which was consistent with the surface results observed by XPS measurement (**Figure 2c**). The Ti–edge EXAFS spectra of C_4-TiO_x is shown in **Figure 2e**, together with the reference samples of TiO_2 and Ti_3SiC_2. The first shell of C_4-TiO_x represented the Ti–O coordination with an average distance of 2.04 Å, which was larger than that of typical Ti–O coordination in TiO_2. Moreover, the coordination number of C_4-TiO_x was fitted to be 4.9 (**Table S1**), which was smaller than that of typical TiO_2. In addition, the Debye–Waller factor of the Ti–O shell for C_4-TiO_x was 0.006 $Å^2$, which was larger than that of TiO_2. This suggested a more distorted octahedral coordination of Ti in C_4-TiO_x, and further indicated that the density of the Ti^{3+} species increased with the increasingly distorted structure (**Table S1**).[33] For the second-shell in **Figure 2e**, Ti_3SiC_2 showed Ti-C-Ti peak at 2.48 Å, and TiO_2 showed Ti-O-Ti peak at 2.71 Å, whilst C_4-TiO_x displayed two peaks at 2.32 Å and 2.82 Å, which could be assigned to the slightly distorted Ti-C-Ti and Ti-O-Ti, respectively.[33] The shifts could be attributed to the local twisting of the bonds, which was associated with the less-crystallized structure of C_4-TiO_x. Therefore the partial oxidization of the exfoliated Ti_3SiC_2 was achieved, and the obtained structure was denoted as C_4-TiO_x. Prior theoretical calculation predicted a strong interaction between N_2 and Ti^{3+} sites in TiO_2, which would greatly facilitate the adsorption and activation of N_2 molecules,[22,24] and thus, would enhance the photocatalytic activity of TiO_2 for the N_2 reduction reaction. The Brunauer–Emmett–Teller surface area of C_4-TiO_x was determined to be 140.2 $m^2\ g^{-1}$, which was approximately 94 times higher than that of Ti_3SiC_2 (1.5 $m^2\ g^{-1}$). Moreover, C_4-TiO_x exhibited a type-IV isotherm (**Figure 2f**),[41] which indicated that the presence of numerous mesopores with less than 50 nm in size, in accordance with the pore size distribution curve (inset in **Figure 2f**). Such large surface area implied the presence of more exposed reaction sites on the surface of the photocatalyst, such as Ti^{3+} and/or

OVs, which likely played key roles for the chemisorption and activation of N_2 as predicted using first principles calculations.[22]

The photocatalytic nitrogen reduction involves four key steps, including charge generation, nitrogen adsorption, the adsorbed nitrogen reduction and the product desorption. To investigate the kinetics of the electron-hole generation after the irradiation of C_4-TiO_x, we observed the electron paramagnetic resonance (EPR) spectra at 105K. Ti_3SiC_2 did not exhibit a resonance signal and TiO_2-air displayed a very weak signal at g = 2.083 assigned to the surface O_2^- ions (**Figure 3a**).[42,43] However, the EPR spectrum of C_4-TiO_x exhibited hyperfine structure, which included both parallel and perpendicular bands. The EPR signal at g = 2.004 was assigned to the electrons trapped by the large number of Ti^{3+} sites at the surface of C_4-TiO_x, which favored the electron transfer to adsorbates during the catalytic process.[22] The EPR signal at g = 2.016 was ascribed to the surface-trapped holes associated with O-centered radicals (*eg.,* O^-), which could react with water and/or the OH^- ions to form OH radicals.[46] Owing to the presence of abundant electron and hole traps (Ti^{3+} sites and O-centered radicals, respectively) in its structure, C_4-TiO_x exhibited strongly quenched PL compared to that of TiO_2-air (**Figure 3b**), which was caused by the greatly suppressed recombination of the photogenerated electron–hole pairs. This efficient charge separation efficiency in turn increased the lifetime of the charge carries (**Figure 3c**) of C_4-TiO_x (6.55 ns) compared to that of TiO_2-air (0.53 ns). These results indicated that the C doping of TiO_2 could readily control the Ti^{3+} sites, which facilitated the effective separation of the electron–hole pairs, thus promising an efficient catalyst for N_2 reduction.

The photocatalytic NH_3 production performance of the C-TiO_x samples was then tested using ion chromatography. The NH_3 synthesis rate of C_4-TiO_x was 26.2 μmol g^{-1} h^{-1} (**Figure 3d**) under visible light irradiation ($\lambda > 420$ nm), which suggested that the Ti^{3+}-containing sample was rather active. To further enhance the photocatalytic activity, Ru species as a reported cocatalyst were directly loaded on the surface of the C-TiO_x *via* a robust photodeposition strategy.[39] The

successful loading of the Ru species was demonstrated using TEM (**Figure S5**), which revealed that the particles presented uniform size (2～3 nm) and were well dispersed through the entire C_4-TiO_x sample. The elementary mapping (**Figure S6**) analysis results revealed the uniform distribution of Ti, O, C, and Ru in C_4-TiO_x. When the amount of Ru species added to C_4-TiO_x was increased from 0 to 5 wt% (**Figure 3d**), the NH_3 production activity of the photocatalysts increased firstly and decreased later. From the XPS results (**Table S2**), the optimum amount of Ru species was determined to be 1.27 at% for the C_4-TiO_x loaded with 5 wt% Ru species (nominal name, Ru 5 wt%/C_4-TiO_x). The strong photoluminescence (PL) quenching of Ru 5 wt%/C_4-TiO_x compared with C_4-TiO_x implied that the recombination of the electron−hole pairs was significantly suppressed (**Figure S7**). The XPS analysis (**Figure S8**) results revealed the presence of two Ru species for Ru 5 wt%/C_4-TiO_x: metallic Ru and RuO_2, which are well-known electron and hole acceptors, respectively.[42,43] Recently, it was also demonstrated that Ru could facilitate the adsorption of N_2.[42] To reveal the real function of Ru species, N_2 temperature programmed desorption (N_2-TPD) analysis was carried out to evaluate the N_2 adsorption capability (**Figure 3e**). Compared to the widely used TiO_2-air photocatalyst, C_4-TiO_x presented extremely high N_2 chemisorption peaks, which strongly indicated that the carbon doped TiO_2 led to the significant increase in the number of active sites for the adsorption of N_2. In addition, the N_2 adsorption capacity of C_4-TiO_x was higher than that of Ru 5 wt%/C_4-TiO_x, which could be attributed to the Ru species partially covering the active adsorption sites of C_4-TiO_x, thus demonstrating that the Ti^{3+} active sites of C_4-TiO_x were more active for the chemisorption of N_2 than Ru, consistent with the predicted property by modelling.[26] This is a very interesting point as Ti^{3+} is superior to Ru which is a widely accepted N_2 adsorption site. Combining with the PL analysis, it can be revealed that Ru and RuO_2 were rationalized to be both charge acceptors and cocatalysts that promoted the separation and mobility of charges.[44-46] In other words, the loading of Ru species on C_4-TiO_x could accelerate charge separation and then the reduction of N_2 instead of increasing the adsorption of N_2. Further increasing the

amount of Ru species caused the NH_3 production rate to decrease (**Figure 3d**), likely due to the excessive amount of Ru species might scatter/absorb photons, which led to the recombination of the surface charge carriers and decrease in the yield of useful carriers (**Figure S9**).[45] These results also indicated that the content of Ru species was not positively correlated with the photocatalytic activity of C_4-TiO_x. It is worth mentioning that, when there is no light, or exposed to light without N_2 or water, scarce NH_3 could be produced as shown in the control experiments in **Figure 3f**, which suggested that NH_3 was synthesized by light-driven N_2 reduction.

To optimize the performance of C-TiO_x, a series of C-TiO_x samples were prepared by changing the H_2O_2-TOE time, and the samples denoted as C_3-TiO_x, C_4-TiO_x, C_6-TiO_x, and C_8-TiO_x, were obtained after 3, 4, 6, and 8 h, respectively (detailed results on other samples except C_4-TiO_x see **Figures S10-S14**). The photocatalytic NH_3 production performance of C-TiO_x samples were tested in the presence of 5 wt% Ru species as cocatalysts (**Figure 4a**). Unlike Ti_3SiC_2 which presented negligible NH_3 production rate, all C-TiO_x samples exhibited higher photocatalytic NH_3 production rates, which decreased as follows: C_4-TiO_x (109.3 μmol g^{-1} h^{-1}) > C_6-TiO_x (74.4 μmol g^{-1} h^{-1}) > C_3-TiO_x (53.2 μmol g^{-1} h^{-1}) > C_8-TiO_x (28.2 μmol g^{-1} h^{-1}), correlated well with the decrease in the coordination number of Ti (**Table S3**). It should be noted that the competitive product of H_2 was too little to be accurately analyzed on the optimized sample. When a 420 nm cut-off filter was used during the photocatalytic synthesis of NH_3, C_4-TiO_x still displayed a remarkable and stable NH_3 production rate of 64.4 μmol g^{-1} h^{-1} (**Figure S15**). The NH_3 production rate of TiO_2-air was approximately 1.0 μmol g^{-1} h^{-1}, much lower than those of all C-TiO_x samples. Interestingly one can find that photocatalytic NH_3 production activity of C-TiO_x was correlated well with the increase in Ti^{3+} concentration (**Figure 4b**), not to C content (**Tables S4, S5**). A close analysis shows that the ratio of Ti^{3+}/Ti^{4+} in the best sample of C_4-TiO_x was as high as 72.1% (**Table S6, S7**), which significantly increased the possibility of adjacent Ti^{3+}. These results indicated that the bottom-up method,

where the special layered Ti_3SiC_2 precursor was used as the flexible feedstock, could be an efficient strategy for the *in situ* preparation and modulation of the Ti^{3+} concentration of the C-TiO_x samples. When Ru 5 wt%/C_4-TiO_x was reused for four cycles, its NH_3 photocatalytic activity did not decrease noticeably (inset in **Figure 4c**), which indicated an excellent stability. The cocatalyst Ru species with a uniform size of 2～3 nm were still distributed evenly on C_4-TiO_x after a long time photocatalytic reaction (**Figure S16**). Simultaneously, the nanosheets structure of C_4-TiO_x can be maintained (**Figure S17a**), and the Ti, C, and O elements were still uniformly distributed in the C_4-TiO_x after long-time run (**Figure S17b**). The Raman spectrum of Ru 5 wt%/C_4-TiO_x after long-time run (**Figure S17c**) remained unchanged compared with its initial state, suggesting its stability. Furthermore, the Ti content, Ti^{3+} concentration and in particular the ratio of Ti^{3+}/Ti^{4+} in the best sample of C_4-TiO_x before and after reaction displayed a negligible change (**Tables S6** and **S7**). All these suggested the robustness of our photocatalyst. The wavelength-dependent NH_3 production data revealed that the catalytic activity of C_4-TiO_x matched its optical absorption spectrum, and thus, suggested that the production of NH_3 was primarily driven by the photoinduced charges (**Figure 4c**). The calculated apparent quantum efficiency of Ru 5 wt%/C_4-TiO_x was 1.1% at 400 nm, much higher than that of the recently reported efficient doped TiO_2 photocatalysts (**Table S8**).[24] We believe this is due to the different concentration of Ti^{3+}, which is highlighted in our work. Furthermore, the NH_3 synthesis rate on C_4-TiO_x using water as the proton source was also measured. It was observed that the NH_3 synthesis rate of C_4-TiO_x was 66.1 μmol g^{-1} h^{-1} (**Figure S18**) under $\lambda > 395$ nm irradiation. Meanwhile, an approximate stoichiometric ratio of O_2 could be detected (**Figure S19**).

To confirm the N source in the formed NH_3, the production of isotopically labeled $^{15}NH^{4+}$ was detected using the indophenol blue method, as illustrated in **Figure S20**.[23,24] Both $^{14}N_2$ and $^{15}N_2$ solutions displayed a unique absorption peak at 630 nm, which was ascribed to the

presence of indophenols in the samples. The solutions were further subjected to time of flight mass spectroscopy (TOF MS) analysis. The ^{14}N-labeled indophenol anion at *m/z* of 198 and strong ^{15}N-labeled indophenol anion at *m/z* of 199 were identified in the spectra of $^{14}NH^{4+}$ and $^{15}NH^{4+}$ solutions, respectively (**Figure 4d**). Additionally, when $^{15}N_2$ was utilized as the N source, the abundance ratio of ^{15}N:^{14}N in the product was significantly higher than that obtained when $^{14}N_2$ was used as the N source, which suggested that N_2 gas was the source of photocatalytically synthesized NH_3.

The ultraviolet–visible (UV–vis) adsorption spectra and XPS valence band (VB) spectra were used to analyze the electronic structure of C_4-TiO_x, Ti_3SiC_2, and TiO_2-air. As shown in **Figure 5a**, the UV–vis spectrum of black Ti_3SiC_2 did not present a noticeable absorption edge in the 250–800nm wavelength range, which suggested its metallic nature and lack of photocatalytic activity.[32,33] The TiO_2-air with a white color exhibited an absorption edge at approximately 395 nm, corresponding to the bandgap of 3.11 eV (**Figure 5b**), which was consistent with the data reported in the literature for anatase TiO_2.[28] The UV–vis spectrum of C_4-TiO_x showed two absorption edges at 407 and 564 nm, which were corresponding to the two bandgaps of C_4-TiO_x at 3.06 and 2.08 eV, respectively, by extrapolating the linear region of the Tauc's plots.[47] These results suggest that the C doping has the main contribution to the enhanced visible absorption and the Ti^{3+} has a minor contribution to the visible absorption. XPS spectra showed the valance band maxima (VBM) of TiO_2-air and C_4-TiO_x were 3.02 and 2.74 eV (**Figure 5c**), respectively, indicating a negative VBM shift of approximately 0.28 eV for C_4-TiO_x due to both its low-degree crystallinity induced distortion and the likely intraband caused by the partially occupied Ti 3d orbital and C 2p orbital.[24,28,48] Moreover, a sub-occupied energy level was observed in the XPS spectrum of C_4-TiO_x, which could be assigned to the C substitution-induced states above the VBM comprising O_{2p} orbitals, resulting into a new energy level of 1.76 eV and a visible responsive band gap of 2.08 eV (**Figure 5b**). These results were consistent with the data reported in the literature for C-doped TiO_2.[28] It was reported that the

VBM of anatase TiO_2 was located at approximately 2.8 eV (*vs.* NHE),[2,24] and therefore, the band alignment of TiO_2-air and C_4-TiO_x is illustrated in **Figure 5d**. The above results indicated that C-doping not only redshifted the absorption edge of C_4-TiO_x toward visible wavelengths, but also favored the formation of high-concentration Ti^{3+} species. Simultaneously, both Ru species favored charge separation and surface catalysis.

Based on the above-mentioned results, we proposed the following mechanism for the photocatalytic production of NH_3. As mentioned above four key steps occur during the reduction of N_2 to NH_3: (i) the generation of charges followed by their migration towards the reaction sites of the photocatalyst, (ii) the chemisorption of N_2 on the surface of the photocatalyst, (iii) the reduction of N_2, and (iv) the desorption of NH_3 from the surface of the photocatalyst. Because it is very difficult for N_2 to be chemically adsorbed on the surface of most oxides, creating a surface of a catalyst enriching N_2 adsorption sites is paramount. Therefore, the superior NH_3 production performance and remarkable stability of C_4-TiO_x could be attributed to the following rationales: (i) C doping could enhance the visible light harvesting of C_4-TiO_x, and facilitat the charge separation, (ii) the strong positive correlation between the concentration of Ti^{3+} sites and photocatalytic activity of C_4-TiO_x suggested the presence of high-concentration Ti^{3+} active sites in C_4-TiO_x which could significantly improve the chemisorption of N_2 and reduce N_2 to ammonia, and (iii) the synergistic effects of the added ultra-small Ru/RuO_2 nanoparticles favored the effective separation of charge carriers and enhanced the catalytic effect of C_4-TiO_x. Moreover, the pore structure of C_4-TiO_x provided more available surface area to reactants, thereby increasing the number of active catalytic sites.

In summary, this work demonstrated the C-TiO_x nanosheets with high-concentration Ti^{3+} were successfully prepared by using Ti_3SiC_2 as the key precursor, which resulted in a significant enhancement for photocatalytic ammonia synthesis. The carbon doping has been proven to induce controllable Ti^{3+} active sites and broad visible light absorption. When further immobilising of Ru/RuO_2 nanoparticles on the C-TiO_x samples, a strong synergistic effect on

the simultaneous enhancement of charge separation and transfer, and the catalytic function has been observed on the $Ru/RuO_2/C\text{-}TiO_x$ samples. Thus they exhibited an outstanding ammonia production rate and photochemical stability, dramatically superior to all the reported TiO_2-based catalysts. In particular a good correction of Ti^{3+} concentration in the $C\text{-}TiO_x$ samples with the NH_3 synthesis rate has been monitored, resulting into 109.3 umol g^{-1} h^{-1} production rate and more importantly 1.1% AQY at 400 nm on the optimized $C_4\text{-}TiO_x$. Furthermore it has been found that Ti^{3+} ions was superior to the widely known Ru catalyst for N_2 adsorption. Therefore this work not only demonstrates the real reaction sites of Ti^{3+} clusters for N_2 photoreduction and for NH_3 production, but also puts forward an attractive bottom-up strategy to prepare C-doped TiO_2 in one step, which could be used in diverse areas, *eg*. solar fuel and environmental purification *etc*.

Supporting Information
Supporting Information is available from the Wiley Online Library or from the author.

Acknowledgements
This work was supported by the NSFC (21575014, 21905025), Beijing Natural Science Foundation (2184122), the Fundamental Research Funds for the Central Universities (2018CX01017), Beijing Institute of Technology Research Fund Program for Young Scholars, the project of State Key Laboratory of Explosion Science and Technology (Beijing Institute of Technology, YBKT18-03), China Scholarship Council, and Analysis & Testing Center, Beijing Institute of Technology. J. W. T., Q. H., H. M. J. and J. J. X are thankful for financial support from UK EPSRC (EP/N009533/1), Royal Society-Newton Advanced Fellowship Grant (NA170422) and the Leverhulme Trust (RPG-2017-122).

Received: ((will be filled in by the editorial staff))
Revised: ((will be filled in by the editorial staff))
Published online: ((will be filled in by the editorial staff))

References

[1] Smil, *Nature* **1999,** *400,* 415.

[2] G. N. Schrauzer, T. D. Guth, *J. Am. Chem. Soc.* **1977,** *99,* 7189.

[3] P. K. Wang, F. Chang, W. B. Gao, J. P. Guo, G. T. Wu, T. He, P. Chen, *Nat. Chem.* **2017,** *9,* 64.

[4] W. B. Gao, J. P. Guo, P. K. Wang, Q. R. Wang, F. Chang, Q. J. Pei, W. J. Zhang, L. Liu, P. Chen, *Nat. Energy* **2018,** *3,* 1067.

[5] S. Licht, B. C. Cui, B. H. Wang, F. F. Li, J. Lau, S. Z. Liu, *Science* **2014,** *345,* 637.

[6] N. Cao,, Z. Chen, K. T. Zang, J. Xu, J. Zhong, J. Luo, X. Xu, G. F. Zheng, *Nat Commun.* **2019,** *10,* 2877.

[7] Y. X. Zhao, R. Shi, X. Bian, C. Zhou, Y. F. Zhao, S. Zhang, F. Wu, G. I. N. Waterhouse, L. Z. Wu, C. H. Tung, T. R. Zhang, *Adv. Sci.* **2019,** *6,* 1802109.

[8] X. Z. Chen, N. Li, Z. Z. Kong, W. J. Ong, X. J. Zhao, *Mater. Horiz.* **2018,** *5,* 9.

[9] T. Oshikiri, K. Ueno, H. Misawa, *Angew. Chem.* **2016,** *128,* 4010.

[10] A. J. Medford, M. C. Hatzell, *ACS Catal.* **2017,** *7,* 2624.

[11] C. H. Hu, J. B. Jin, Y. Han, S. M. Chen, H. X. Ju, J. Cai, Y. R. Qiu, C. Gao, C. M. Wang, Z. M. Qi, R. Long, L. Song, Z. Liu, Y. J. Xiong, *J. Am. Chem. Soc.* **2019,** *141,* 7807.

[12] J. W. Bao, E. A. Carter, *J. Am. Chem. Soc.* **2019,** *141,* 13320.

[13] J. Yang, Y. Guo, R. Jiang, F. Qin, H. Zhang, W. Lu, J. Wang, J. Yu, *J. Am. Chem. Soc.* **2018,** *140,* 8497.

[14] S. Zhou, X. W. Yang, X. Xu, S. X. Dou, Y. Du, J. Zhao, J. *J. Am. Chem. Soc.* **2020,** *142,* 308.

[15] H. Li, J. Shang, Z. H. Ai, L. Z. Zhang, *J. Am. Chem. Soc.* **2015,** *137,* 6393.

[16] S. Y. Wang, X. Hai, X. Ding, K. Chang, Y. G. Xiang, X. G. Meng, Z. X. Yang, H. Chen, J. H. Ye, *Adv. Mater.* **2017,** *29,* 1701774.

[17] N. Zhang, A. Jalil, D. D. Wu, S. M. Chen, Y. F. Liu, C. Gao, W. Ye, Z. M. Qi, H. X. Ju, C. M. Wang, X. J. Wu, L. Song, J. F. Zhu, Y. J. Xiong, *J. Am. Chem. Soc.* **2018,** *140,* 9434.

[18] X. L. Xue, R. P. Chen, H. W. Chen, Y. Hu, Q. Q. Ding, Z. T. Liu, L. B. Ma, G. Y. Zhu, W. J. Zhang, Q. Yu, J. Liu, J. Ma, Z. Jin, *Nano Lett.* **2018,** *18,* 7372.

[19] T. T. Hou, Y. Xiao, P. X. Cui, Y. N. Huang, X. P. Tan, X. S. Zheng, Y. Zou, C. X. Liu, W. K. Zhu, S. Q. Liang, L. B. Wang, *Adv. Energy Mater.* **2019,** *9,* 1902319.

[20] Y. F. Zhao, Y. X. Zhao, G. I. N. Waterhouse, L. R. Zheng, X. Z.Cao, F. Teng, L. Z. Wu, C. H. Tung, D. O'Hare, T. R. Zhang, *Adv. Mater.* **2017,** *29,* 1703828.

[21] W. K. Wang, H. M. Zhang, S. B. Zhang, Y. Y. Liu, G. Z. Wang, C. H. Sun, H. J. Zhao, *Angew. Chem. Int. Ed.* **2018,** *58,* 16644.

[23] H. Hirakawa, M. Hashimoto, Y. Shiraishi, T. Hirai, *J. Am. Chem. Soc.* **2017,** *139,* 10929.

[22] C. C. Li, T. Wang, Z. J. Zhao, W. M. Yang, J. F. Li, A. Li, Z. L. Yang, G. A. Ozin, J. L. Gong, *Angew. Chem. Int. Ed.* **2018,** *57,* 5278.

[24] Y. X. Zhao, Y. F. Zhao, R. Shi, B. Wang, G. I. N. Waterhouse, L. Z. Wu, C. H. Tung, T. R. Zhang, *Adv. Mater.* **2019,** *31,* 1806482.

[25] B. Comer, A. J. Medford, *ACS Sustainable Chem. Eng.* **2018,** *6,* 4648.

[26] N. Cao, Z. Chen, K. T. Zang, J. Xu, J. Zhong, J. Luo, X. Xu, G. F Zheng,. *Nat. Commun.* **2019,** *10,* 2877.

[27] B. M. Comer, Y. H. Liu, M. B. Dixit, K. B. Hatzell, Y. F. Ye, E. J. Crumlin, M. C. Hatzell, A. J. Medford, *J. Am. Chem. Soc.* **2018,** *140,* 15157.

[28] S. U. Khan, M. A. Al-Shahry, W. B. Ingler Jr., *Science* **2002,** *297,* 2243.

[29] C. D. Valentin, G. Pacchioni, A. Selloni, *Chem. Mater.* **2005,** *17,* 6656.

[30] V. Nicolosi, M. Chhowalla, M. G. Kanatzidis, M. S. Strano, J. N. Coleman, *Science* **2013,** *340,* 1226419.

[31] X. T. Wang, W. X. Shi, S. X. Wang, H. W. Zhao, J. Lin, Z. Yang, M. Chen, L. Guo, *J. Am. Chem. Soc.* **2019,** *141,* 5856.

[32] Q. X. Liu, L. H. Ai, J. Jiang, *J. Mater. Chem. A* **2018,** *6,* 4102.

[33] M. Alhabeb, K. Maleski, T. S. Mathis, A. Sarycheva, C. B. Hatter, S. Uzun, A. Levitt, Y. Gogotsi, *Angew. Chem. Int. Ed.* **2018,** *57,* 5444.

[34] Q. Xue, H. J. Zhang, M. S. Zhu, Z. X. Pei, H. F. Li, Z. F. Wang, Y. Huang, Y. Huang, Q. H. Deng, J. Zhou, S. Y. Du, Q. Huang, C. Y. Zhi, *Adv. Mater.* **2017,** *29,* 1604847.

[35] V. M. Ng, H. Huang, K. Zhou, P. S. Lee, W. X. Que, Z. C. Xu, L. B. Kong, *J. Mater. Chem. A* **2017,** *5,* 3039.

[36] Y. Liao, J. Qian, G. Xie, Q. Han, W. Q. Dang, Y. S. Wang, L. L. Lv, S. Zhao, L. Luo, W. Zhang, H. Y. Jiang, J. W. Tang, *Appl. Catal. B: Environ.* 2020, **273**, 119054.

[37] J. R. Ran, G. P. Gao, F. T. Li, T. Y. Ma, A. J. Du, S. Z. Qiao, *Nat. Commun.* **2017**, *8,* 13907

[38] Q. X. Liu, L. H. Ai, J. Jiang, *J. Mater. Chem.* A **2018**, *6,* 4102.

[39] Y. N. Jiang, T. Sun, X. Xie, W. Jiang, J. Li, B. B. Tian, C. L. Su, *ChemSusChem* **2019**, **12**, 1368.

[40] T. M. Su, Z. D. Hood, M. Naguib, L. Bai, S. Luo, C. M. Rouleau, I. N. Ivanov, H. B. Ji, Z. Z. Qin, Z. L. Wu, *ACS Appl. Energy Mater.* **2019**, *2,* 4640.

[41] Q. Han, Z. H. Cheng, J. Gao, Y. Zhao, Z. P. Zhang, L. M. Dai, L. T. Qu, *Adv. Funct. Mater.* **2017,** *27,* 1606352.

[42] S. M. Prokes, J. L. Gole, X. Chen, C. Burda, W. E. Carlos, *Adv. Funct. Mater.* **2005,** *15,* 161.

[43] C.P. Kumar, N. O. Gopal, T. C. Wang, M. S. Wong, S. C. Ke, *J. Phys. Chem. B* **2006,** *110,* 5223.

[44] J. M. Lee, E. K. Mok, S. Lee, N. S. Lee, L. Debbichi, H. Kim, S. J. Hwang, *Angew. Chem. Int. Ed.* **2016,** *55,* 8546.

[45] N. N. Rao, S. Dube, M. P. Natarajan, *Appl. Catal. B* **1994,** *5,* 33.

[46] H. H. Duan, J. C. Liu, M. Xu, Y. F. Zhao, X. L. Ma, J. C. Dong, X. S. Zheng, J. W. Zheng, C. S. Allen, M. Danaie, Y. K. Peng, T. Issariyakul, D. L. Chen, A. I. Kirkland, J. C. Buffet, J. Li, S. C. Tsang, D. O'Hare, *Nat. Catal.* **2019,** *2,* 1078.

[47] Q. Han, C. G. Hu, F. Zhao, Z. P. Zhang, N. Chen, L. T. Qu, *J. Mater. Chem. A* **2015,** *3,* 4612.

[48] M. Mehta, N. Kodan, S. Kumar, A. Kaushal, L. Mayrhofer, M. Walter, M. Moseler, A. Dey, S. Krishnamurthy, S. Basu, A. P. Singh, *J. Mater. Chem. A* **2016,** *4,* 2670.

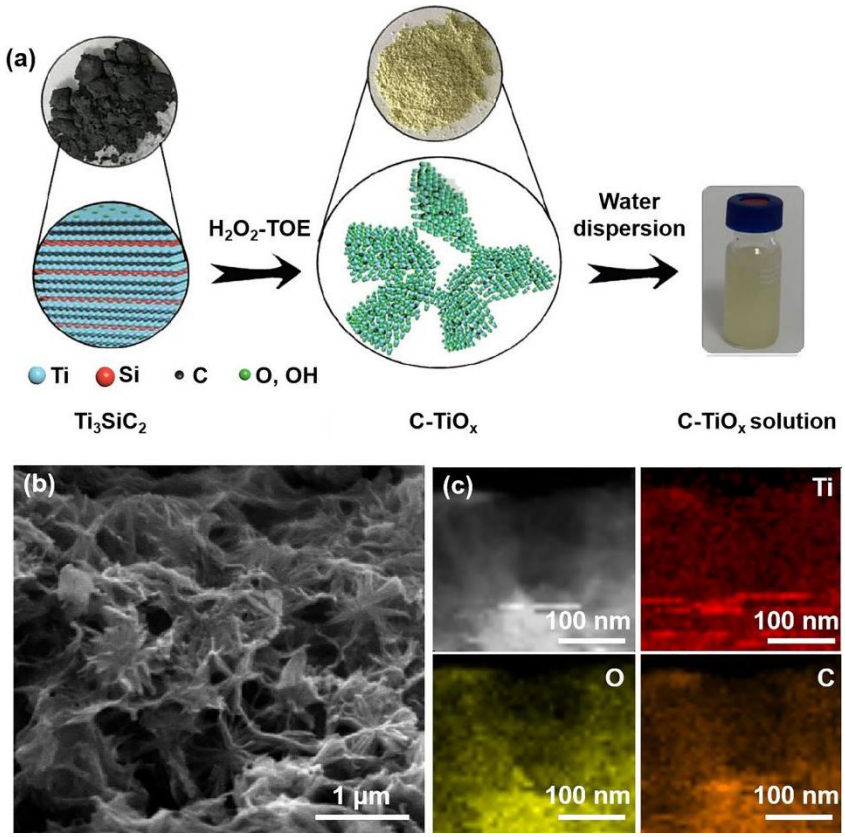

Figure 1. a) The preparation process of C-TiO_x. SEM images of b) C_4-TiO_x. c) High-angle annular dark-field scanning transmission electron microscopy (HAADF-STEM) image with corresponding EDX element mappings of C_4-TiO_x, showing the distribution of Ti, O, and C.

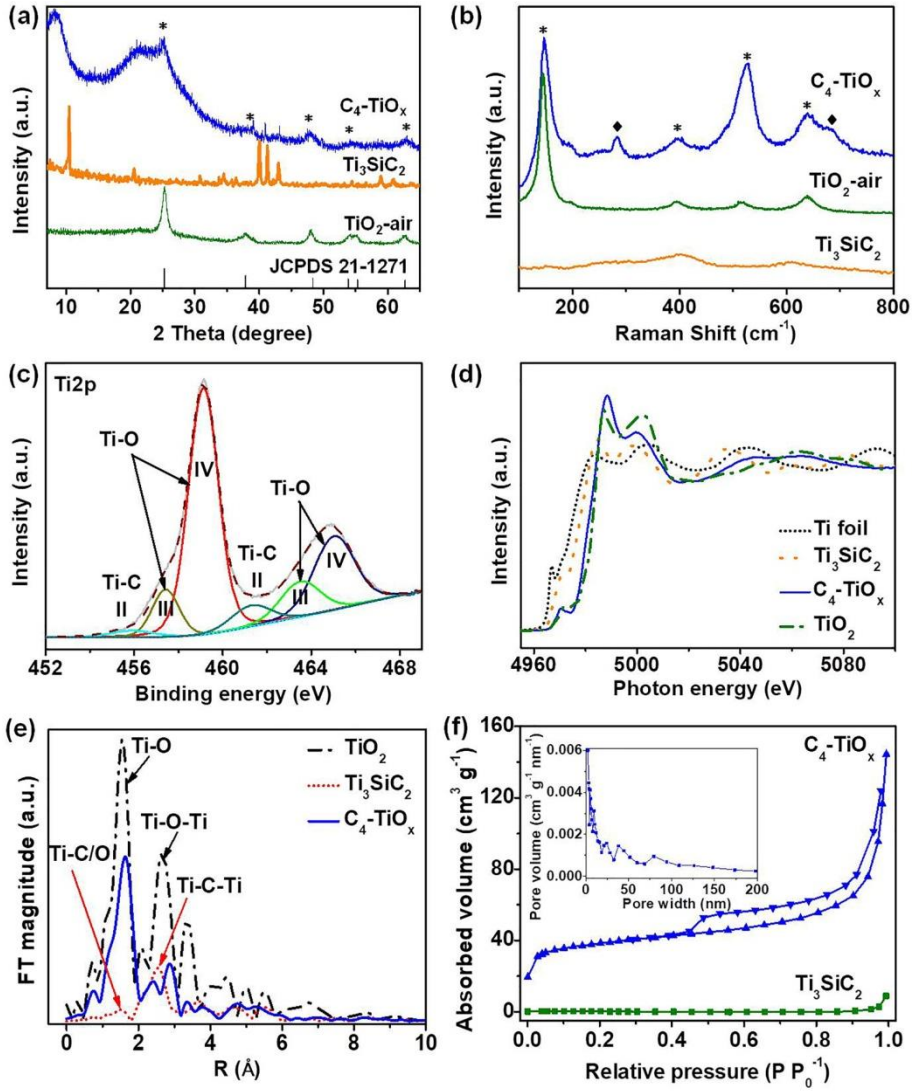

Figure 2. a) XRD patterns and b) Raman spectra of Ti_3SiC_2, C_4-TiO_x, and TiO_2-air. c) High-resolution XPS spectra of Ti *2p* for C_4-TiO_x. d) Ti K-edge XANES spectra of Ti foil, Ti_3SiC_2, C_4-TiO_x, and reference anatase TiO_2. e) Fourier transformed (FT) k^3-weighted of Ti K-edge Extended X-ray Absorption Fine Structure (EXAFS) spectra of Ti_3SiC_2, C_4-TiO_x, and the reference anatase TiO_2. f) N_2 adsorption isotherms of C_4-TiO_x and Ti_3SiC_2. The insert in (f) is pore size distribution curve of C_4-TiO_x.

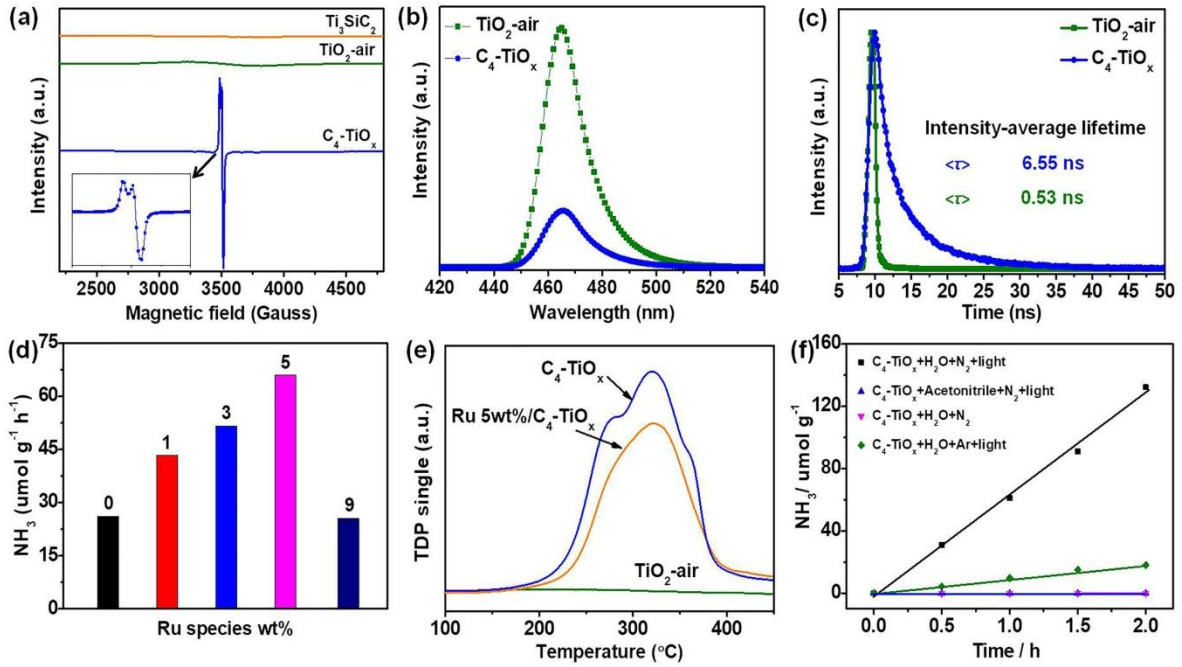

Figure 3. a) Low-temperature EPR spectra of Ti_3SiC_2, TiO_2-air and C_4-TiO_x under light irradiation. Insert: the enlarged view of C_4-TiO_x. b) PL spectra of TiO_2-air and C_4-TiO_x. c) Time-resolved PL spectra TiO_2-air and C_4-TiO_x. d) Photocatalytic NH_3 production rate detected by ion chromatography on different catalysts under visible light irradiation ($\lambda > 420$ nm). e) Temperature-programmed desorption of N_2 on TiO_2-air and C_4-TiO_x, and Ru 5wt%/ C_4-TiO_x. f) Control experiments and photocatalytic NH_3 production on C_4-TiO_x under different reaction conditions ($\lambda > 420$ nm).

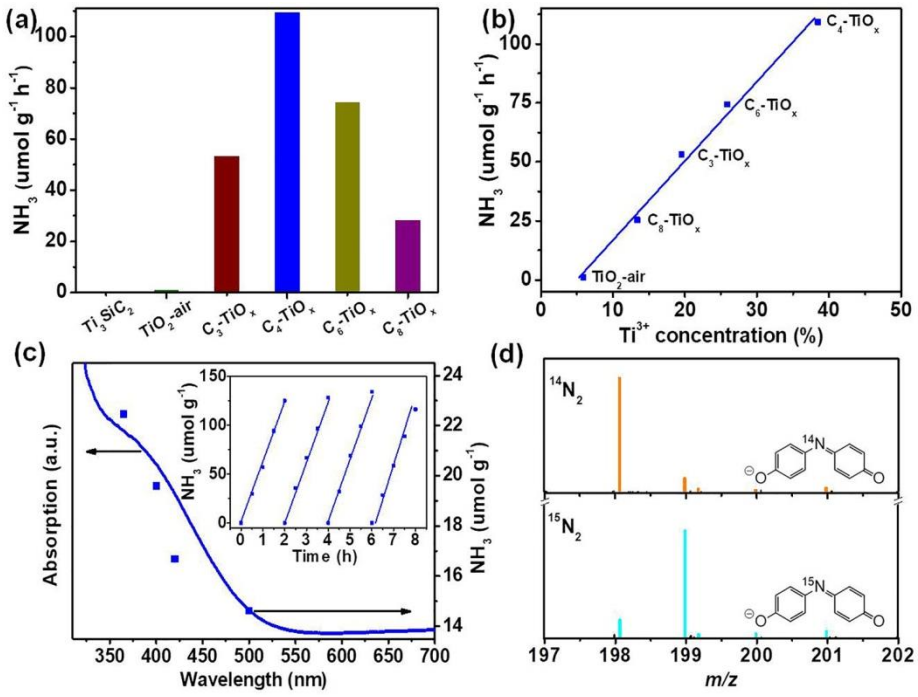

Figure 4. a) Photocatalytic NH_3 production rate detected by Ion chromatography on different catalysts loaded with norminal 5 wt%, Ru species cocatalyst under visible irradiation ($\lambda > 395$ nm). b) Correlation of Ti^{3+} concentration with the yield of NH_3. c) The absorption spectrum of C_4-TiO_x and wavelength dependence of NH_3 production rate on Ru 5wt%/C_4-TiO_x. Inset in (c)

is the stability test of Ru 5wt%/C_4-TiO_x ($\lambda > 420$ nm). d) Isotopic measurement: mass spectra of indophenols in the solutions obtained by the reaction with $^{14}N_2$ and $^{15}N_2$, respectively.

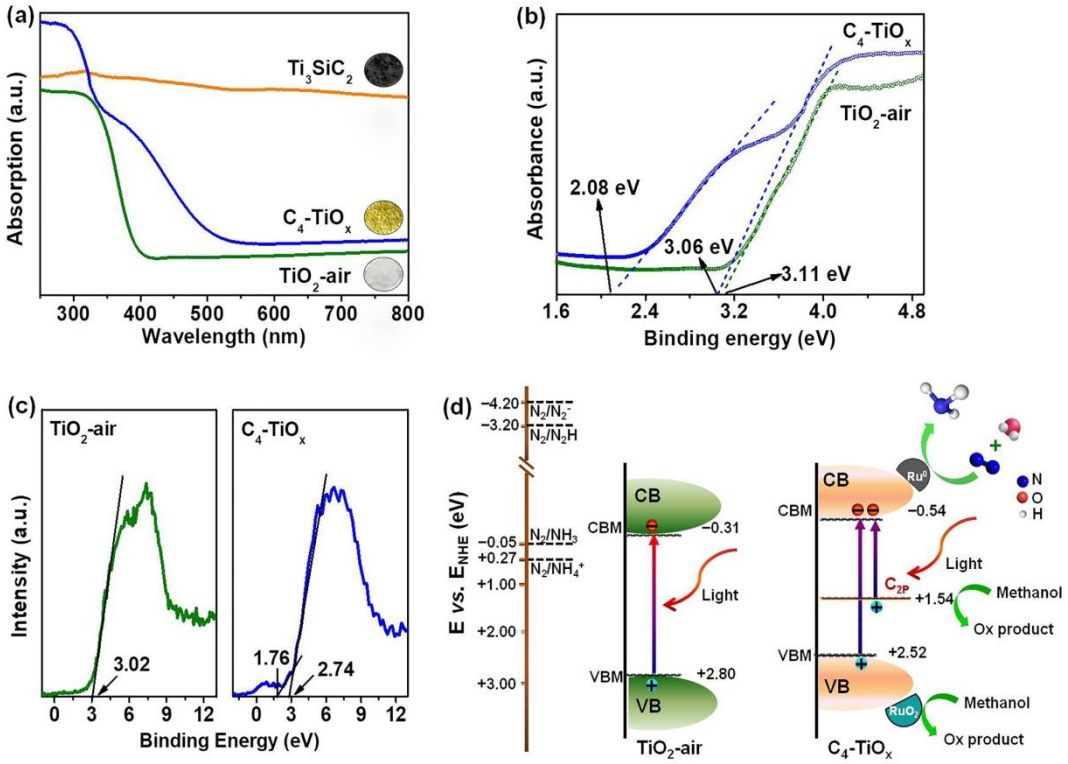

Figure 5. a) UV-vis absorption spectra and photographs of Ti_3SiC_2, TiO_2-air and C_4-TiO_x. b) Tauc plots and c) Valence band (VB) spectra of TiO_2-air and C_4-TiO_x. d) Electronic band structure of TiO_2-air and C_4-TiO_x, and mechanism for photocatalytic NH_3 production on Ru/RuO_2 nanoparticels-loaded C_4-TiO_x under visible light illumination.

The table of contents entry.

A porous carbon-doped anatase TiO_x (C-TiO_x) nanosheet with controllable Ti^{3+} concentration was prepared by a reproducible bottom-up strategy. The optimal C-TiO_x with a high-concentration Ti^{3+} exhibits a NH_3 production rate of 109.3 umol g^{-1} h^{-1} under visible-light irradiation and a remarkable apparent quantum efficiency of 1.1 % at 400 nm, the highest compared with all TiO_2-based photocatalysts.

Keywords
porous carbon-doped TiO_x nanosheets, high-concentration Ti^{3+}, bottom-up strategy, visible light, photocatalytic ammonia synthesis

Q. Han,* C. B. Wu, H. M. Jiao, R. Y. Xu, Y. Z. Wang, J. J. Xie, Q. Guo, J. W. Tang*

Title
Rational Design of High-Concentration Ti^{3+} in Porous Carbon-Rich TiO_x Nanosheets for Efficient Photocatalytic Ammonia Synthesis

ToC figure